Interpretable crack features for the representation of kinematic fields in the case of fatigue overloads

Ghita Bahaj Filali, Michel Coret, Adrien Leygue, Julien Réthoré

To cite this version:

Ghita Bahaj Filali, Michel Coret, Adrien Leygue, Julien Réthoré. Interpretable crack features for the representation of kinematic fields in the case of fatigue overloads. International Journal of Fracture, 2025, ⟨10.1007/s10704-024-00830-2⟩. ⟨hal-04496354v3⟩

HAL Id: hal-04496354

https://hal.science/hal-04496354v3

Submitted on 22 Jan 2025

Interpretable crack features for the representation of kinematic fields in the case of fatigue overloads

Ghita BAHAJ FILALI[1*], Michel CORET[1†], Adrien LEYGUE[1†], Julien RÉTHORÉ[1†]

[1*]Nantes Université, École Centrale Nantes, CNRS, GeM, UMR 6183, [F-44300] , France.

*Corresponding author(s). E-mail(s): ghita.bahaj-filali@ec-nantes.fr; Contributing authors: michel.coret@ec-nantes.fr; adrien.leygue@ec-nantes.fr; julien.rethore@ec-nantes.fr;
†These authors contributed equally to this work.

Abstract

Purpose: many engineering structures are subjected to variable amplitude loading. A number of studies investigate the effects of post overload, even-though it is crucial to describe what occurs during the overloading. The aim of this paper is to provide effective independent descriptors based on purely kinematic measurements for the analysis of overloading.
Methods: fatigue tests were conducted on a SENT specimen. Investigating crack propagation was through direct measurements using Digital Image Correlation (DIC) and Linear Elastic Fracture Mechanics (LEFM) via Williams' series expansion. The higher terms in Williams' series expansion, referred to as crack features were analyzed in cycles with and without overload.
Results: in a case without overload, all features exhibit a proportional regime. Singular Value Decomposition (SVD) analysis confirms that a single feature is adequate to characterize the mechanism. In a cycle with overload, the regime changes during the overloading phase, making it a signature of this phase. In this case, the SVD analysis reveals that two descriptors are needed for these cycles. A subsequent analysis allows the definition of two physically interpretable features.
Conclusion: this work presents a robust method to identify, based on kinematic measurements and SVD analysis, independent descriptors for the processes that occur during a cycle with overload. [*]

Keywords: Fatigue overloads, DIC, Williams' series, Dimensionality reduction

---

1 Introduction

In engineering, the prediction of the service life of components and structures is necessary to ensure safety. Enhancing the capacity to withstand diverse loading conditions can be regarded as a primary focus of engineering research. Reflecting real-world and complex conditions, cyclic loading can be considered one of the most studied loading types. Such repeated cyclic loading can cause fatigue cracking within structural components. This phenomenon can be particularly challenging to predict and manage, making it a central concern in engineering disciplines [15, 20]. For most of these components, real loading cycles involve variable amplitude rather than constant amplitude loading. Hence the study of overloads is important to understand their signature.

The effects of single peak tensile overloads have already been widely investigated [14, 16, 19] as this form of loading may result in significant load interaction effects. Several mechanisms have been proposed, based on Linear Elastic Fracture Mechanics (LEFM), to explain crack growth retardation post overload. These include models based on residual stresses [13], crack closure [6], strain hardening [5], crack branching [18] and reversed yielding [12].

Fatigue life prediction in this case is complex because most of the studies used the empirical Paris' law [7]. This law establishes a direct correlation between the stress intensity factor range (ΔK) as single crack feature and the crack growth rate per cycle ($\mathrm{d}a/\mathrm{d}N$), and has been widely applied to model fatigue crack growth during constant amplitude loading. However, Paris' law exhibits several limitations, specifically it only models the stable crack propagation, and does not consider the stress ratio effects [17]. Many other fatigue crack propagation laws have been proposed to overcome the limitations of the Paris law and also to deal with variable amplitude loading [1]. The proposed fatigue models differ on the number of features involved and the number of parameters required to be identified through curve fitting.

This work aims to provide independent kinematic descriptors for the mechanisms that occurs during the overload. For this purpose, local and direct optical measurements of the displacement fields obtained through digital image correlation (DIC) during overload are analysed through LEFM via Williams' series expansion. The Series coefficients provide a first set of kinematic crack features. These are then further reduced to two interpretable features using data analysis and dimensionality reductions tools. This paper is structured as follows: in section 2 we presented the experimental set-up, including material, loading condition and specimen geometry. The DIC for measuring kinematic fields and Williams' series expansion are recalled. Crack features are presented in section 3 and then analyzed qualitatively in section 4. In section 5 a quantitative, Singular Value Decomposition (SVD)-based, analysis was carried out. The last section is a summary of the presented study.

2 Raw data

2.1 Fatigue test on a SENT specimen

The specimen is made of Al-7%Si cast alloy with an average grain size of 150 μm. Eutectic Si particles are dispersed in a globular shape obtained by coalescence following heat treatment (the material is provided by Centre Technique des Industries Mécaniques CETIM). The elastic material properties are the Young's modulus (E) of 74 GPa and the Poisson's ratio (ν) of 0.3. Experiments are done on a Single Edge Notched Tension (SENT) specimen. The geometry is defined in Figure 1.

The fatigue test was conducted in mode I, the specimen contains an initial notch at the border perpendicular to the tensile axis. The initial length of the notch is $a_0 = 3$ mm, then the crack propagates through the whole specimen, until complete failure. All experiments were performed using an electro-magnetic machine (Instron ElectroPuls E10000) with a load cell of 10 kN maximum loading capacity and a frequency of f=20 Hz.

Preliminary experiments have been conducted, leading to the choice of a cycling range between F_{min}=1kN and F_{max}=7kN. The choice of the overloading load was a compromise between the maximum capacity of the machine and a significant overloading load, thus F_{ovl}=1.25F_{max}.

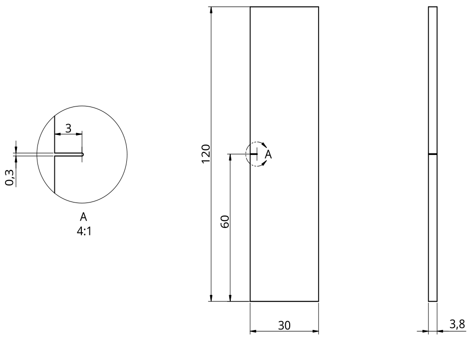

Fig. 1: SENT specimen geometry (dimensions in mm).

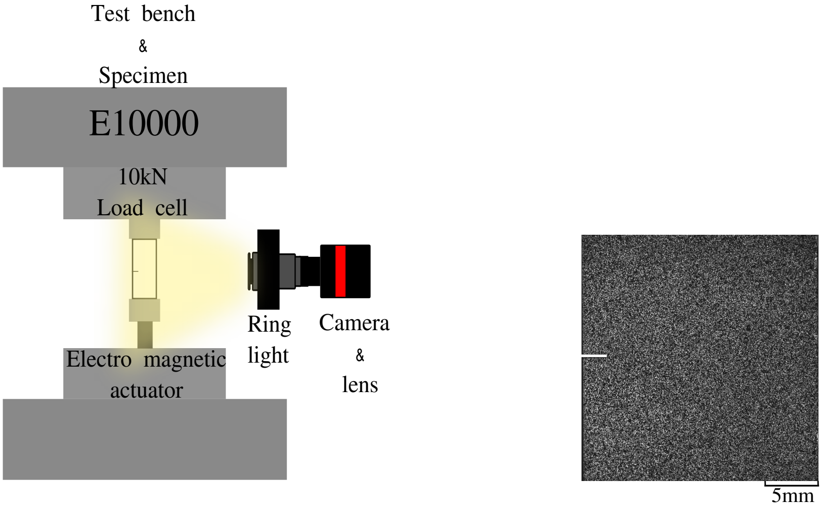

(a) Schematic view (b) Speckle pattern

Fig. 2: Experimental setup

Table 1 Optical system and patterning technique

Camera	47 Megapixel Vieworks
Image resolution	7920×6004
Lens	TOKINA 100 mm
Aperture	f/2.8
Field of view	38.7×23.3 mm
Image scale	1 px = 4.8μm
Patterning technique	Spray paint (can + airbrush)

The experiment was divided into two stages:

- **Initiation.** The sample was subjected to cyclic tensile loading, the aim was to achieve a crack length of 3 mm which was reached after 60000 cycles. This crack length is sufficient to mitigate the influence of the notch during the initiation of the crack.
- **Propagation plus overload stage.** After the pre-cracking stage, when crack propagation was deemed sufficient, an overload was applied to the sample. Once the crack has resumed growing, after 1100 cycles, the process of applying an overload and letting the crack grow again is repeated until the sample breaks (Figure 3).

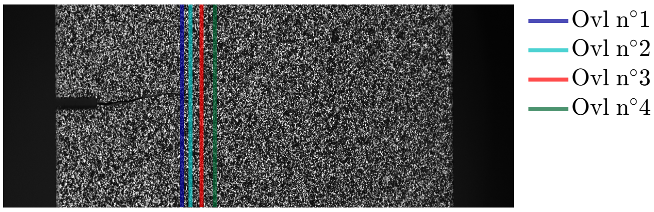

Fig. 3: Overload positions in the sample

During the experiment, pictures were taken for future DIC analyses. The images were captured using a 47 Megapixels Vieworks camera equipped with a 100 mm lens (Tokina). The lighting of the sample was ensured by a LED ring light (FPR-136BL2 by CCS Inc). A black and white speckle pattern is painted on the specimen using cans and an airbrush. The experimental setup can be seen in Figure 2, camera specifications are presented in Table 1.

An image of the unloaded and uncracked specimen is first taken. Then, during the pre-cracking stage, images were captured each 5000 cycles at F_{max}. During propagation and overloading, images were taken each 0.5 kN from F_{min} to F_{max} and each 0.25 kN from F_{max} to F_{ovl} (Figure 4).

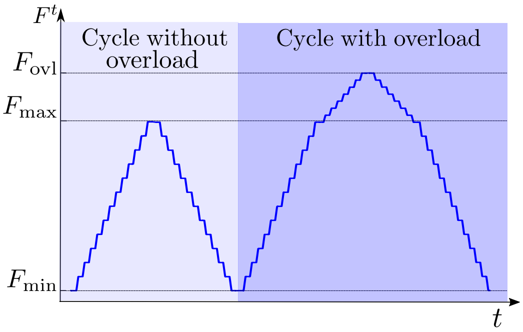

Fig. 4: Image acquisition strategy. Each image is taken at a constant force.

All the images taken during experiments were used for DIC processing. DIC is a full-field method that involves analysing a series of images to extract displacement fields. The displacement field $\underline{u}_{\text{DIC}}$ is computed between an undeformed image I_0 and a deformed one I_1. This displacement field is estimated following the optical flow equation 1:

$$I_0(\underline{X}) = I_1(\underline{X} + \underline{u}_{\text{DIC}}(\underline{X})). \tag{1}$$

The measurement of the displacement is an ill-posed problem. It is solved iteratively in the least squares sense using a Finite Element (FE) discretization [2] implemented in UFreckles software [11]. The displacement field is decomposed over a regular mesh of 4-node bilinear quadrangular elements. A median filter with the 1st neighbours was used to reduce the impact of noise while preserving discontinuities (Table 2).

Table 2 DIC software parameters

Software	UFreckles [11]
Shape function	Bi-linear quadrilateral Lagrange element (Q4P1)
Element size	[20 20] px^2 / [0.097 0.097] mm^2
Post-filtering	Median filter using 1st neighbours

2.2 Pre-overload and overload analysis

For all this study, cycles were analysed independently. For each cycle we computed the variation of the load related to F_{min} as follows:

$$\delta_t F = F^t - F_{\text{min}},$$

and the variation of the displacement field also related to the displacement at F_{min} as follows:

$$\delta_t \underline{U} = \underline{U}^t - \underline{U}^{F_{\text{min}}},$$

with $\underline{U}^t$ and F^t is the t^{th} displacement vector and load respectively in the loading range ($F_{\text{min}} \leq F^t \leq F_{\text{ovl}}$ in both loading and unloading phase) and $\underline{U}^{F_{\text{min}}}$ the displacement field at F_{min}.
The variation of the vertical component of the displacement vector field is depicted for 4 cycles with overload at F_{ovl} and the cycle right before each overload at F_{max} (Table 3). Note that the displacement amplitudes shown in this Table exceed the typical measurement error in DIC that is known to be around 0.01 px. For every overload, the displacement magnitude increases in comparison to the precedent cycle, this increase is expected because the load is proportional to displacement magnitude. A projection onto Williams' series expansion was then performed using these displacement fields, leading to the extraction of crack features.

2.3 Asymptotic displacement using Williams' series

Williams [21] provides the asymptotic representation of the displacement field near a crack tip in linear elastic isotropic materials. The power of Williams series expansion is the preeminent asymptotic description of the displacement fields near a crack tip in the conventional LEFM.
The 2D displacement field is expressed in the polar coordinate system crack tip

Table 3 Vertical component of the displacement field in [px] at δF_{ovl} (right) and $\delta F_{\max}$ (left) for cycles with overload and their precedent respectively. Here 1 px=4.8μm.

Ovl n°	$\delta F_{\max}$	δF_{ovl}
1	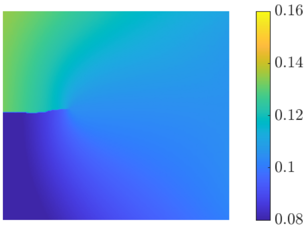	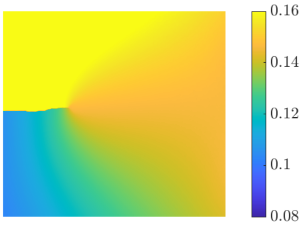
2	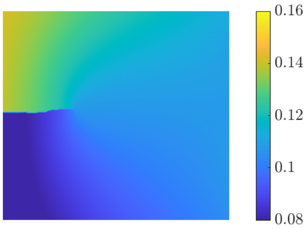	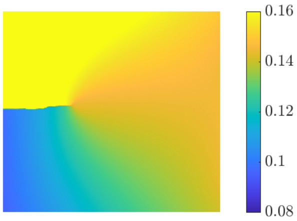
3	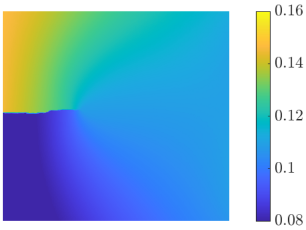	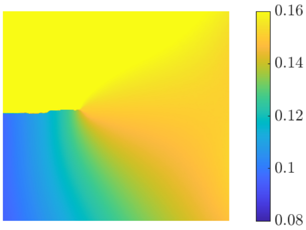
4	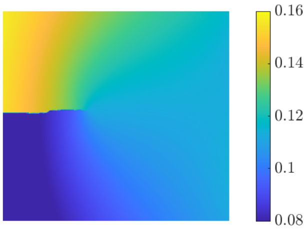	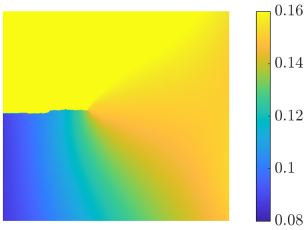

centered as follows (Figure 5):

$$\delta_t \underline{U}_W(r,\theta) = \sum_{n=-\infty}^{+\infty} \delta_t a_I^n \underline{\phi}_I^n(\theta) r^{\frac{n}{2}}, \tag{2}$$

with $\delta_t a_I^n$ Williams' coefficients and $\underline{\phi}_I^n$ a base function. $\underline{\phi}_I^n(\theta)$ is expressed in a complex basis with i the complex number as follows:

$$\underline{\phi}_I^n = \frac{1}{\mu\sqrt{8\pi}}\left[\kappa e^{\mathrm{in}\theta/2} - \frac{n}{2}e^{\mathrm{i(4-n)}\theta/2} + \left(\frac{n}{2} + (-1)^n\right)e^{-\mathrm{i(4-n)}\theta/2}\right], \tag{3}$$

with $\mu = \frac{E}{2(1+\nu)}$ =28.46 GPa, ν=0.3 and $\kappa = \frac{3-\nu}{1+\nu}$=2.07, representing the shear modulus, Poisson's ratio, and Kolossov's constant under plane stress assumption, respectively.

Negative values of n are typically disregarded because they would lead to an infinite strain energy density at the crack tip. However, the crack tip position being unknown, the first supersingular term ($n = -1$) is used to estimate the position to the equivalent elastic crack tip along a pre-defined crack path [3]. In the vicinity of the crack tip, $n = 0$ refers to the rigid body translations, $n = 1$ (δK_{I}) to singular stress, $n = 2$ (δT) to the uniform stress and $n = 3$ (δB) to the third term in the Williams series.

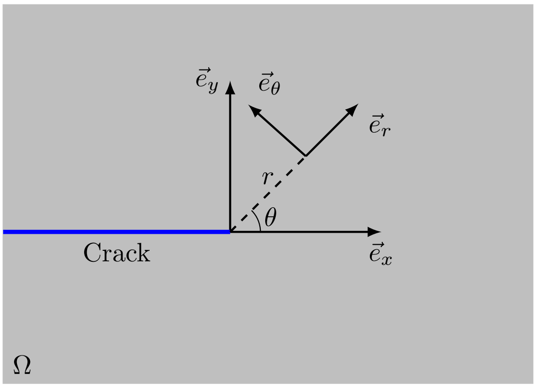

Fig. 5: Cartesian and cylindrical coordinate system around the crack tip in a solid Ω.

2.4 Crack features extraction

In order to convert the DIC displacement fields in the dictionary of LEFM defined by the Williams' series, a projection (in the least square sense) of $\delta\underline{U}_{\mathrm{DIC}}$ onto the analytical expression was performed and different fracture mechanics features was derived (e.g. $\delta_t K_{\mathrm{I}}$, δ_tT, δ_tB and crack tip position)[8–10]. The following objective function (eq. 4) was minimized:

$$\delta_t a_I^n = \arg\min_{\delta_t a_I^n}\{\|\delta\underline{U}_{\mathrm{DIC}} - \delta\underline{U}_{\mathrm{W}}(\delta_t a_I^n)\|_2\} \tag{4}$$

where $\|\delta\underline{U}_{\mathrm{DIC}} - \delta\underline{U}_{\mathrm{W}}\|_2$ refers to the norm over all the nodes.
The projection domain, as illustrated in Figure 6, is an annulus characterized by its external and internal radii, denoted as r_{ext}=2.4 mm and r_{int}=0.29 mm. A region above and below the crack faces of r_{int} width is also excluded as the FE DIC does

not describe explicitly the displacement discontinuity. The internal radius r_{int} was considered to exclude the close vicinity of the crack tip where DIC may be less reliable and because the use of supersingular terms would lead to an ill-conditioned projection matrix. The external radius r_{ext} has to be small enough to avoid influences of the free boundaries, but large enough to include sufficient mesh points in the domain. The right size of the projection domain, i.e. defining r_{ext} and r_{int}, has been identified through a parametric study ensuring that the values of crack features are not sensitive to the size of the projection domain. One would consider a criterion based on the size of the K-dominance zone. However, the size of this zone is difficult to estimate and in practice it may change in size and shape as the crack propagates. A more pragmatic approach based on a parametric study was thus preferred.

Equation 2 affirms, that displacements can be computed for an infinite sum of modes. However, limiting the solution from $n_{\text{min}} = -3$ to $n_{\text{max}} = 7$ is sufficient to retain the relevant crack parameters [4].

Thus, the displacement field in mode I around the crack tip can be written as follows:

$$\begin{aligned}
\delta_t \underline{U}_{\text{W}} = & \sum_{n_{\text{min}}}^{-1} \underbrace{\delta_t a_I^n \underline{\phi}_I^n(\theta) r^{\frac{n}{2}}}_{\text{supersingular terms}} + \underbrace{\delta_t a_I^0 \underline{\phi}_I^0(\theta)}_{\text{translation}} \\
& + \underbrace{\delta_t a_I^1 \underline{\phi}_I^1(\theta)\sqrt{r}}_{\text{singular term}} + \sum_{2}^{n_{\text{max}}} \underbrace{\delta_t a_I^n \underline{\phi}_I^n(\theta) r^{\frac{n}{2}}}_{\text{subsingular terms}} \\
= & \sum_{n_{\text{min}}}^{-1} \underbrace{\delta_t a_I^n \phi_I^n(\theta) r^{\frac{n}{2}}}_{\text{supersingular terms}} + \underbrace{\delta_t a_I^0 \underline{\phi}_I^0(\theta)}_{\text{translation}} \\
& + \underbrace{\delta_t K_I \underline{\phi}_I^1(\theta)\sqrt{r}}_{\text{singular term}} \\
& + \underbrace{\delta_t T \underline{\phi}_I^2(\theta) r + \delta_t B \underline{\phi}_I^3(\theta) r^{\frac{3}{2}} + \sum_{4}^{n_{\text{max}}} \delta_t a_I^n \underline{\phi}_I^n(\theta) r^{\frac{n}{2}}}_{\text{subsingular terms}}
\end{aligned} \tag{5}$$

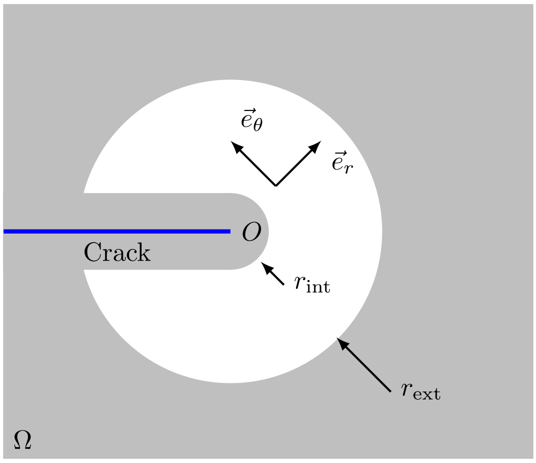

Fig. 6: Projection domain defined by r_{ext} the external radius and r_{int} the internal radius.

3 Results

3.1 Residual displacement analysis

An examination of the projection quality is necessary to validate the features extraction. Thus we propose the following indicator:

$$\alpha = \frac{\|\delta \underline{U}_{\text{DIC}} - \delta \underline{U}_{\text{W}}\|_2}{N_{nodes}} \times \frac{\Delta F}{\delta_t F},$$

with $\Delta F = F_{\max} - F_{\min}$.
α is a measure of the normalized average nodal residual displacement amplitude. It is scaled by $\frac{\Delta F}{\delta_t F}$ to account for the increase of the displacement magnitude with the load $\delta_t F$. It is therefore, a good candidate to quantify the quality of features extraction and displacement field reconstruction.

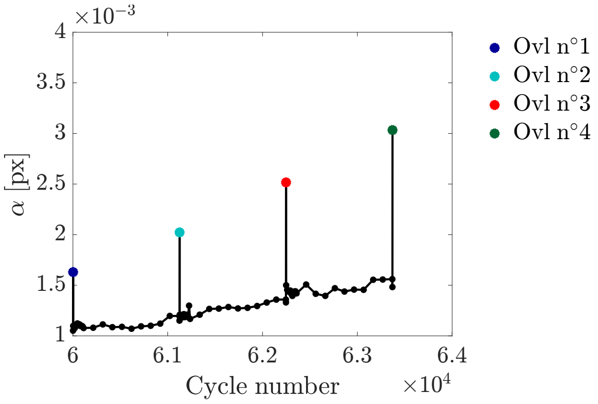

Fig. 7: Normalized average nodal residual displacement amplitude α in [px] as a function of the number of cycles. Here 1 px=4.8μm.

Figure 7 shows α as a function of the number of cycles during the loading phase, 4 peaks corresponding to 4 overloads are seen. The figure depicts an upward tendency. Due to the crack propagation, the displacement magnitude increases and thus α also. However the values are below 0.01 pixel which, in view of displacement values observed in Table 3, means that the reconstruction of the displacement fields from Williams' series was very accurate.

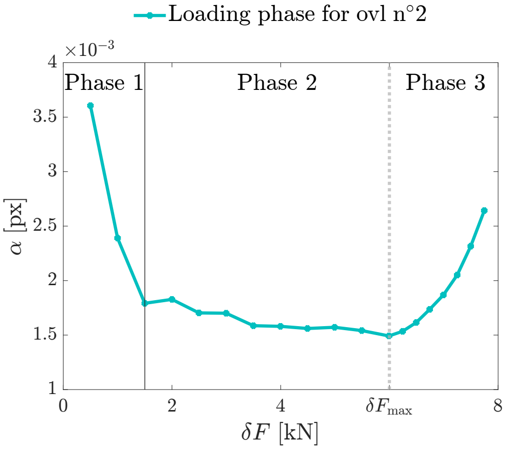

Fig. 8: Example of a normalized average nodal displacement error amplitude α in [px] as a function of the load for the second overload in the loading phase. Here 1 px=4.8μm.

Figure 8 depicts α as a function of the load during the loading phase of a cycle with overload. Here, three phases are seen. Phase 1 shows a significant decrease in α, which can be explained by the fact that δF grows from zero while the measured displacement grows from a small but finite value. In Phase 2, we observe a plateau, indicating that the average extraction residual is proportional to the displacement magnitude (or equivalently the applied load). Finally, in Phase 3, which is the overloading phase, we notice an increase in α and it is probably due to the significant displacement magnitudes or partly because Williams' series could be less appropriate to reconstruct the displacement during overload. However, all values remain below 0.01 pixel which means that the features are successfully extracted even in the overloading phase. This analysis thus proves that, even if Williams' series are based on linear elasticity, they can capture the effects of non-linear phenomena, in the vicinity of the crack tip, on the kinematic field inside the projection domain that is expected to cover a region where the material remains elastic.

3.2 Crack features

Here, we choose to present 3 crack features (δK_{I}, δT and δB), the 4 others are presented in the Appendix section in Figure A1. These features are presented in the following plots (Figure 9 and Figure 10) depicting their evolution upon δF for 4 cycles with overload and the cycle just before each overload. For these plots, continuous lines are used for the loading phase while dashed lines denotes the unloading phase.

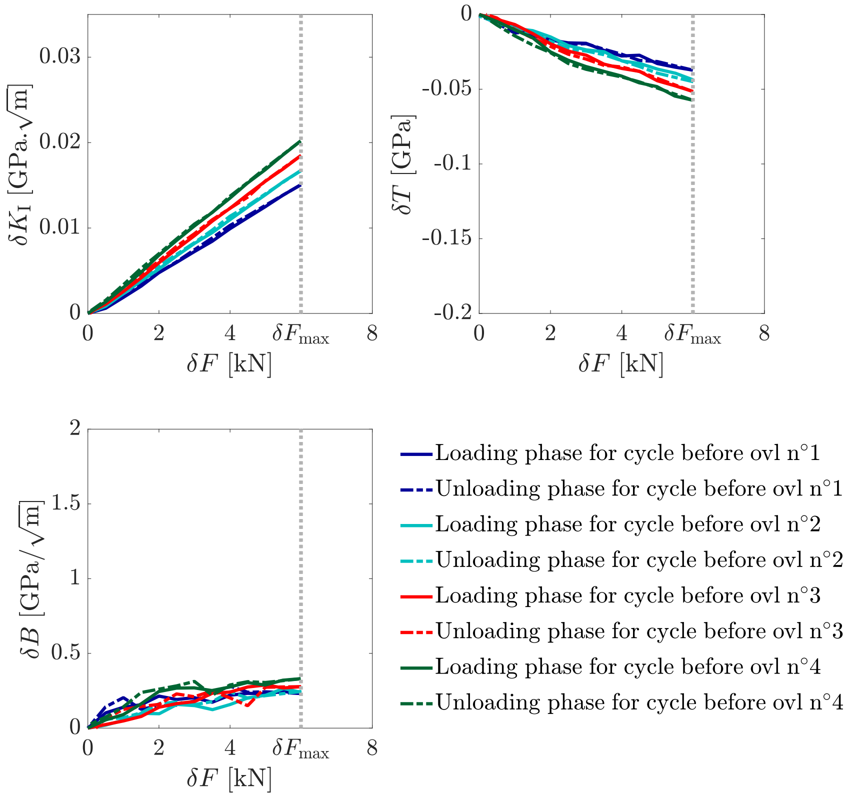

Fig. 9: Crack features (δK_{I}, δT and δB) as a function of the δF for the cycle right before each overload

Figure 9 shows the features as a function of the load. The same behavior can be seen for all features, they exhibit a single regime where they are all proportional to δF both during loading and unloading phase. The slope value of these features increase from an overload to the other, reflecting the growing displacement magnitude caused by crack propagation. δB is less smooth than δK_{I} and δT. These observations are consistent with LEFM assumptions.

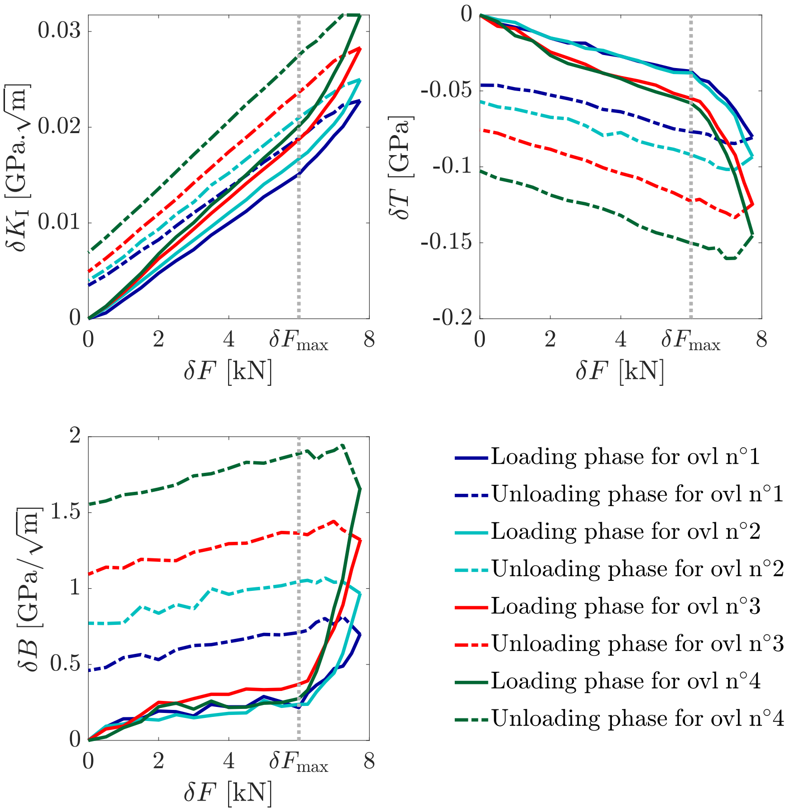

Fig. 10: Crack features (δK_{I}, δT and δB) as a function of δF for cycles with overload

Figure 10 shows crack features as a function of the load δF during cycles with overload. The same behavior is observed for the three features. The loading phase (from $F_{\min}$ to $F_{\max}$) shows a proportional regime to δF. This regime changes during the overloading phase (from $F_{\max}$ to F_{ovl}), here crack features increase faster than δF making this growth an overload signature. The unloading phase is linear with δF, it apparently maintains the same slope as observed during the loading phase. However, at the end of the cycle, while the load is relaxed, persistent crack features values are obtained. This is to be related to the effect of the accumulated plastic strain in the vicinity of the crack tip.

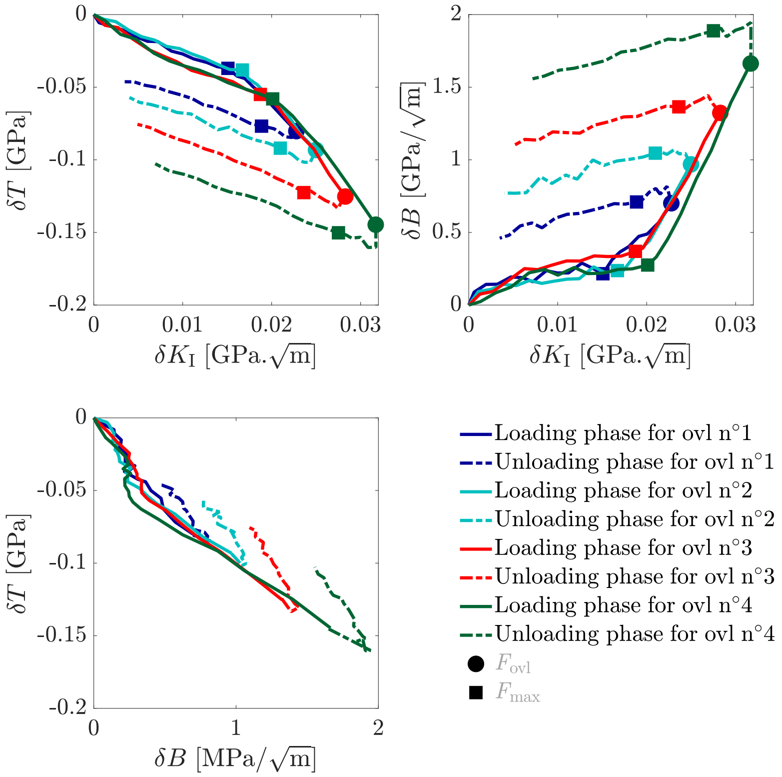

Fig. 11: $(\delta K_{\mathrm{I}}, \delta T)$, $(\delta K_{\mathrm{I}}, \delta B)$ and $(\delta B, \delta T)$ plots for cycles with overload

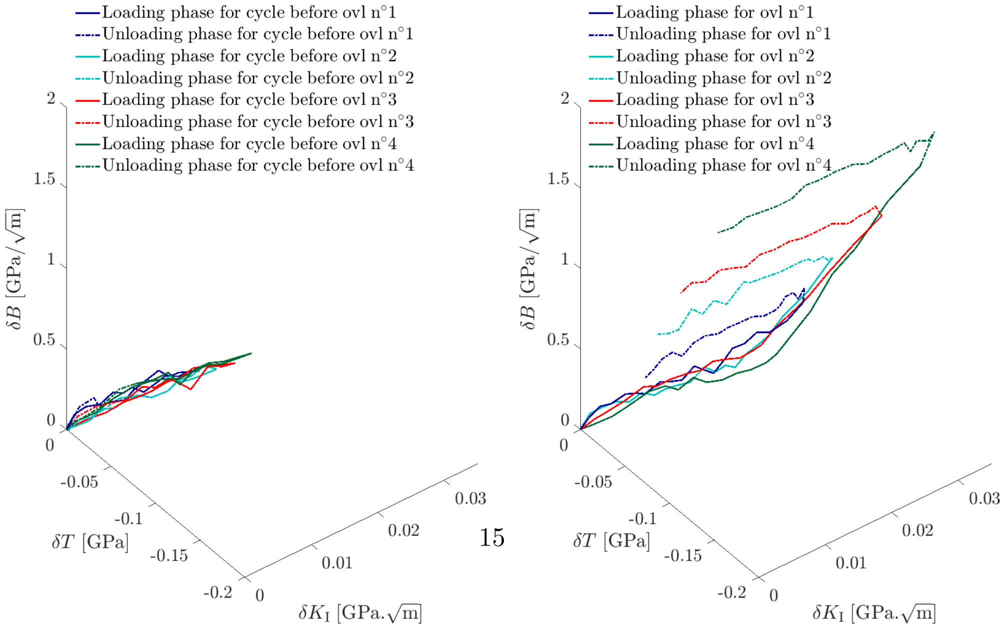

(a) (b)

Fig. 12: 3D representation of δK_{I} , δT and δB for cycles before overload (a) and during overload (b)

Figure 11 shows δT as a function of δK_{I} and δB as a function of δK_{I}, during the loading phase δT and δB depicts respectively a proportional regime to δK_{I}, then this regime changes during the overloading phase where δT and δB grows faster than δK_{I}. The unloading phase maintains almost the same slope as observed during the loading phase. The two hysteresis shows that in a case of a cycle with overload δT and δB are not proportional to δK_{I}.
The third plot shows δT against δB, a strong correlation is observed between the two features. These three plots suggests that δK_{I} is an independent feature, while δT and δB are dependent on each other.
To better understand the link, Figure 12 shows the crack features state representation in the $(\delta K_{\mathrm{I}}, \delta T, \delta B)$ space during a cycle without overload (a) and with overload (b). In a case without overload a clear line is observed, signifying, as observed previously, that all the crack features are proportional to each other. In a case with overload the crack features coordinates seem to lie in a plane. In these two distinct cases, qualitatively different structures are observed. In the next section, we will analyze these geometries and propose an appropriate basis to describe each of them.
All the data presented above are available on zenodo website (doi: 10.5281/zenodo.10795209).

4 Analysis

4.1 Singular Value Decomposition

As strong correlations are observed among the previously identified features, we propose an analysis based on the Singular Value Decomposition (SVD) to further reduce the number of relevant features. The SVD is carried out on a rectangular matrix A_{ft} that gathers for a single cycle all the features at all time steps. The line index f corresponds to the singular and subsingular coefficients in Williams' series expansion $\delta_t a_I^f$ with f ranging from $f = 1$ to $f = 7$. The column index t corresponds to the loading steps with t ranging from $t = 1$ to $t = 26$ in a case without overload and and $t = 39$ otherwise. The rank of the matrix A_{ft} is therefore at most 7. Additionally, each line of A_{ft} is rescaled to make it dimensionless:

$$A_{ft} = \delta_t a_I^f \cdot \frac{r_c^{\frac{f}{2}-1}}{E}, \tag{6}$$

where $r_c = r_{\max}$ is a characteristic length and E is the Young's modulus.

The SVD of A_{ft} can be written as follows:

$$A_{ft} = \sum_{i=1}^{\mathrm{rank}(A_{ft})} U_f^{(i)} \sigma^{(i)} V_t^{(i)}, \tag{7}$$

with

- $\sum_f U_f^{(i)} \cdot U_f^{(j)} = \delta_{ij}$ and $U_f^{(i)}$ is the i^{th} left singular vector,

- $\sigma^{(i)} \geq \sigma^{(j)} \quad \text{for} \quad \mathrm{i} < \mathrm{j}$ and $\sigma^{(i)}$ is the i^{th} singular value,
- $\sum\limits_t V_t^{(i)} \cdot V_t^{(j)} = \delta_{ij}$ and $V_t^{(i)}$ is the i^{th} right singular vector.

Before analyzing the decomposition, the reconstruction error is computed. From the SVD it is indeed possible to compute $\tilde{A}_{ft}^k$, the best rank-k approximation of A_{ft} as:

$$\tilde{A}_{ft}^k = \sum_{i=1}^{k} U_f^{(i)} \sigma^{(i)} V_t^{(i)} \ , \tag{8}$$

with $k \leq \mathrm{rank}(A_{ft})$. The relative approximation error in Fröbenius norm, ranging from 0 (k=rank(A_{ft})) to 1 ($k = 0$), writes:

$$e(k) = \frac{||A_{ft} - \tilde{A}_{ft}^k||_{\mathrm{F}}}{||A_{ft}||_{\mathrm{F}}} = \frac{\sqrt{\sum_{i=k+1}^{\mathrm{rank}(A_{ft})} \sigma^{(i)2}}}{\sqrt{\sum_{i=1}^{\mathrm{rank}(A_{ft})} \sigma^{(i)2}}} \ . \tag{9}$$

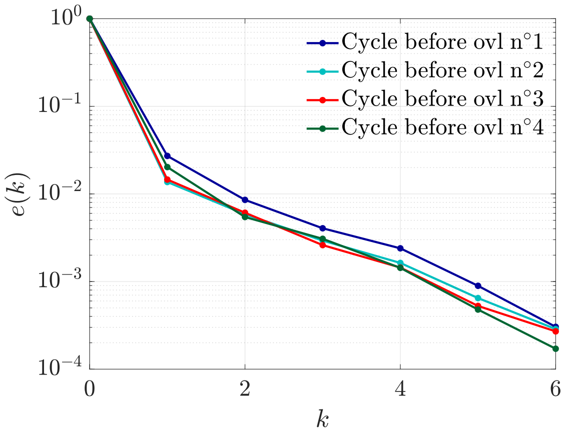

(a) Cycles before overload

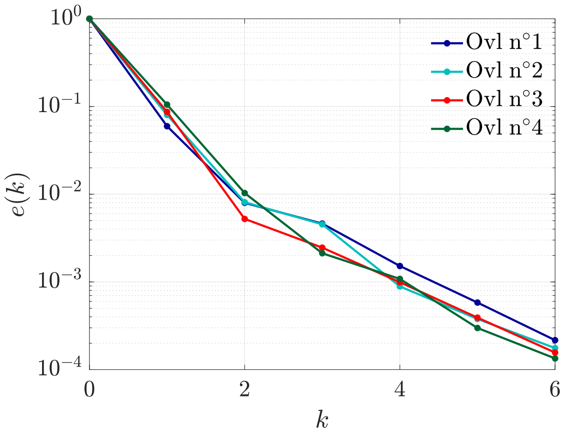

(b) Cycles with overload

Fig. 13: Relative approximation error versus the number of terms k

Figure 13 shows the relative approximation error as a function of k. For cycles without overload, the relative error drops below 1% with just a single term. Adding more terms has a limited effect as illustrated by the slope reduction beyond $k = 1$. This suggests that a single term is adequate for accurately describing the matrix A_{ft} in a cycle without overload. This was expected because the crack features are proportional to each other as seen in Figure 12 (a). For cycles with overload, two terms are needed to reach approximately a relative error of 1%. This corresponds also to a slope change in the reconstruction error which means that an additional descriptor is needed compared to the previous case. This confirms and generalizes the observation made in Figure 12 (b): all the points which co-ordinates in the space of the $\delta_t a_I^f$ Williams' coefficients are defined in A_{ft} approximately lie on a plane generated by the orthogonal basis $\left(U_f^{(1)}, U_f^{(2)}\right)$. To validate this approximation, we defined, in Equations (10, 11, 12), $\delta_t\tilde{K}_{\mathrm{I}}$, $\delta_t\tilde{T}$ and $\delta_t\tilde{B}$ the SVD reconstruction of the crack features as follows:

$$\delta_t\tilde{K}_I = \tilde{A}_{1t}^{(2)} \cdot \frac{E}{r_c^{\frac{-1}{2}}}, \tag{10}$$

$$\delta_t\tilde{T} = \tilde{A}_{2t}^{(2)} \cdot E, \tag{11}$$

$$\delta_t\tilde{B} = \tilde{A}_{3t}^{(2)} \cdot \frac{E}{r_c^{\frac{1}{2}}}. \tag{12}$$

A comparison with the original crack features is shown in Figure 14. Other crack features (from $n = 4$ to $n = 7$) are shown in the appendix section in Figure A1.

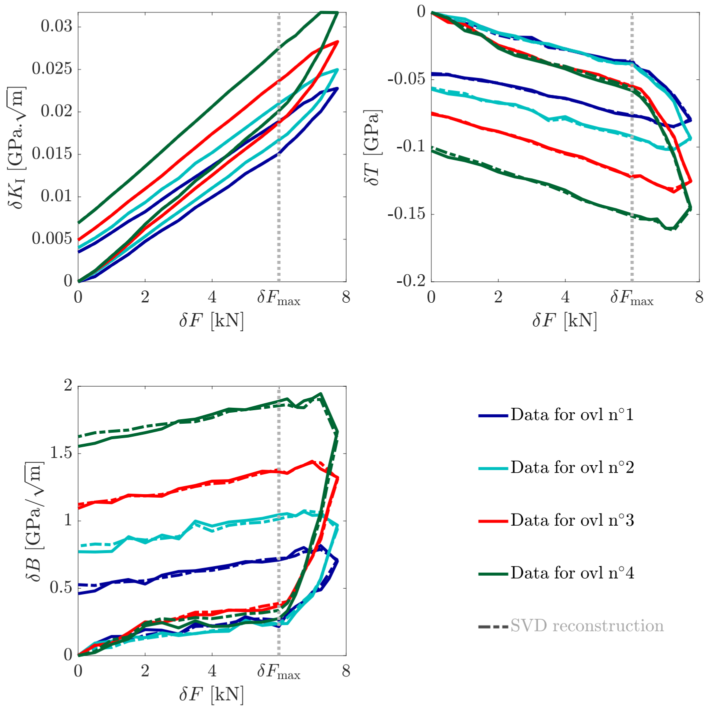

Fig. 14: Crack features (δK_{I}, δT and δB) and their SVD reconstruction ($\delta\tilde{K}_{\mathrm{I}}$, $\delta\tilde{T}$ and $\delta\tilde{B}$) as a function of δF for cycles with overload

We can clearly see that the SVD reconstruction of the crack features is accurate. For δK_{I}, it is difficult to distinguish between the reconstructed data and the original data. Tiny differences exist for δT. Finally, the rank 2 reconstruction smoothes δB for $\delta F \leq \delta F_{\max}$. For the cycles without overload, the evolution of the crack tip state is obviously dominated by δK_{I}. Its contribution $U_1^{(1)}$ to the single mode required for a robust reconstruction of the crack feature evolution is around 99%. Analyzing the results of the SVD for the cycles with overload allows to obtain the two linear combinations of the original crack features describing the evolution of the crack tip state in the most condensed but robust way (as shown by the low reconstruction errors). As illustrated in Figure 15, the first mode defined by $U_f^{(1)}$ is similar for all the overload cycles and is dominated by the contribution of δK_{I} ($f = 1$) but still contains some contribution of δT ($f = 2$) and δB ($f = 3$). Concerning the second left singular vector $U_f^{(2)}$, the main contribution comes from the second and third crack features, namely δT and δB. This change in the number of required left singular vectors when analyzing cycles without overload and cycles with overload and their coordinates in the crack features space, unquestionably suggests that δK_{I} cannot be considered as the unique descriptor of the kinematic field around the crack tip when an overload is applied. This also suggests that additional sub-singular terms must be included to properly describe the crack tip kinematic field.

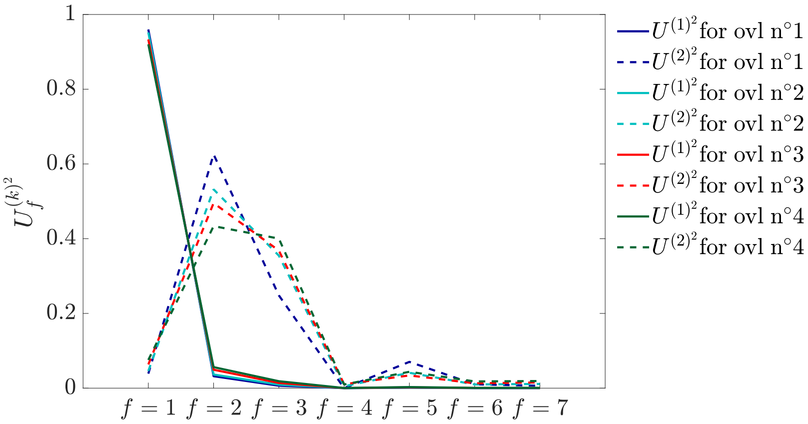

Fig. 15: $U_f^{(k)^2}$ for $k = 1$ and $k = 2$ for all cycles with overload

4.2 Evolution of the crack tip state

An other interesting point is that, from Figure 16, the amplitude of the second singular value $\sigma^{(2)}$ grows faster, between overloads, than the amplitude of the first singular value $\sigma^{(1)}$. This suggests that the increase in crack length induces an increase in the contribution of the second singular value compared to the first one.

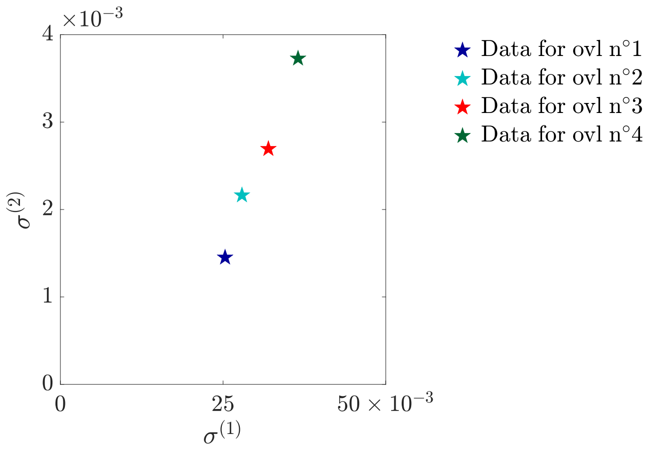

Fig. 16: $\sigma^{(2)}$ as a function $\sigma^{(1)}$ for all cycles with overload

Let us remind that the two vectors $\left(U_f^{(1)}, U_f^{(2)}\right)$ actually define a basis of the best approximating plane, in the 7 dimensional space of the crack features, to the data contained in A_{ft}. Figure 12 clearly illustrates the existence of this plane in the $(\delta K_{\mathrm{I}}, \delta T, \delta B)$ space. The strong, but not perfect correlation between δT and δB observed in Figure 11 suggested that the normal to this plane is not in the $(\delta T, \delta B)$ plane. This is confirmed by the analysis of the two dominant left singular vectors of the SVD $U_f^{(1)}$ and $U_f^{(2)}$ which both contain a non-vanishing contribution of δK_{I} $(f = 1)$. The evolution of the crack tip state in terms of the two dominant left singular vectors is now analysed in this plane. For this purpose, the trajectories in the $\left(U_f^{(1)}, U_f^{(2)}\right)$ plane, defined by $\left(\sigma^{(1)} V_t^{(1)}, \sigma^{(2)} V_t^{(2)}\right)$ are plotted in Figure 17. It is clearly observed that the trajectories are similar up to a scaling respectively defined by $\sigma^{(1)}$ and $\sigma^{(2)}$ along the two directions. As the crack propagates from the first overload to the fourth one, we observe that $\sigma^{(1)}$ and $\sigma^{(2)}$ increase at different rates (see Figure 16) making this change in the trajectories different along $U_f^{(1)}$ and $U_f^{(2)}$. To further confirm that the crack tip loading paths, once represented in the plane defined by the two dominant left singular vectors $U_f^{(1)}$ and $U_f^{(2)}$, is of the same nature, the trajectories defined by $\left(V_t^{(1)}, V_t^{(2)}\right)$ are plotted in Figure 18. With this representation of the data, it is clear that the crack tip loading path (the evolution of the crack features with respect to δF) is the same irrespective of the crack length. Indeed, as a master curve emerges from $\left(V_t^{(1)}, V_t^{(2)}\right)$, we confirm the unique nature of the crack features evolution when it is presented in the appropriate space. The crack tip loading path is defined by two parallel linear branches for $\delta F \leq \delta F_{\max}$ and a third smooth branch joining the first two ones during the overloading phase.

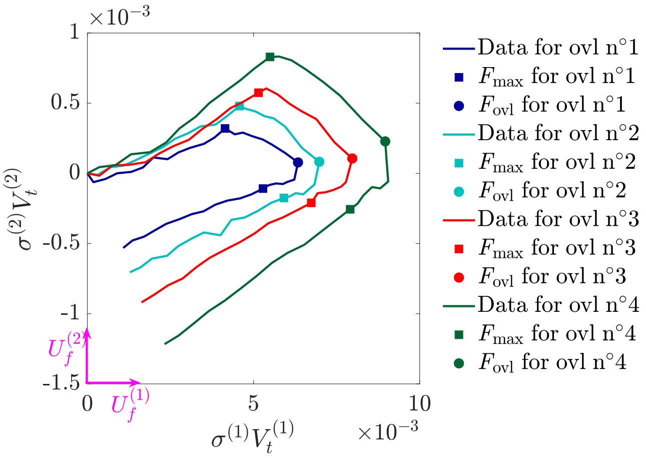

Fig. 17: $\sigma^{(2)}V_t^{(2)}$ as a function $\sigma^{(1)}V_t^{(1)}$ for all cycles with overload expressed in the $\left(U_f^{(1)},U_f^{(2)}\right)$ basis

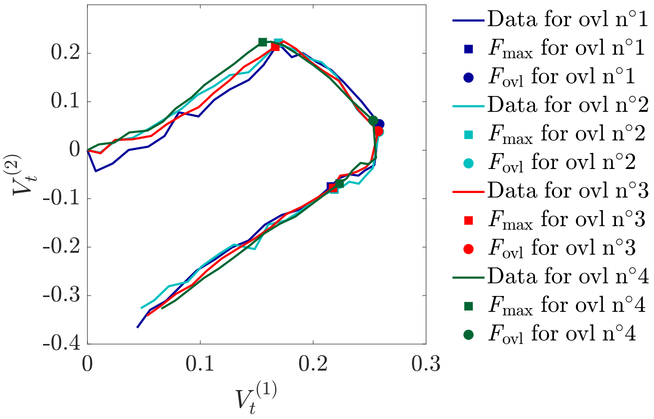

Fig. 18: $V_t^{(2)}$ as a function $V_t^{(1)}$ for all cycles with overload

5 Discussion: towards a constitutive description of crack tip states

From the crack features evolution during cycles with and without overload presented in Section 3, the use of a SVD allows us to extract the main characteristics of the evolution of the kinematic field around the crack tip. For the cycles without overload, it is confirmed that considering a single descriptor, that can be considered to be δK_{I}, is enough. Conversely, non-singular terms must be considered when an overload is applied. Two linear combinations $\left(U_f^{(1)}, U_f^{(2)}\right)$ of crack features (vectors in the crack features space) must actually be considered in this case. If the crack tip loading path is considered in the plane defined by these two vectors a non-proportional loading (trajectories in $\left(V_t^{(1)}, V_t^{(2)}\right)$ plotted in Figure 18) is obtained. The intensities of the loading along these two elementary path descriptors are however different when their evolution with the crack length is considered (see Figure 16).

In the proposed analysis, the SVD is performed independently for each loading cycle. As observed in Figure 15, the coordinates of $\left(U_f^{(1)}, U_f^{(2)}\right)$ in the crack features space are slightly changed from one overload to the next one. Thus, while the interpretation in terms of loading paths defined by the two dominant modes, see trajectories in $\left(V_t^{(1)}, V_t^{(2)}\right)$ is unquestionable, the contribution of these 2 modes once translated into a displacement basis (thanks to the original Williams' functions) is not that straightforward. Part of these changes in $\left(U_f^{(1)}, U_f^{(2)}\right)$ can be attributed to the increase of the crack length, the dependency of $\delta K_{\mathrm{I}}/\delta F$, $\delta T/\delta F$ and $\delta B/\delta F$ and all the other crack features per unit load with respect to the crack length being different and dependent on the specimen geometry. Also, as illustrated in Figure 19, the evolution of the contribution of the two right singular vectors $\left(V_t^{(1)}, V_t^{(2)}\right)$ with the applied load δF is non-linear. This means that the non-linear evolution of the crack features with δF, see Figure 11, is reported on the two dominant left singular vectors $\left(U_f^{(1)}, U_f^{(2)}\right)$. With this respect, the interpretation of the respective contribution of $U_f^{(1)}$ and $U_f^{(2)}$ is difficult. In particular it is not possible at that point to separate the displacement around the crack in a mode evolving linearly with δF (expected to be the same as for the case without overload and to be dependent only on the crack length) and another one holding the non-linear dependence on δF. It also makes difficult to interpret the different evolution of the singular values $\sigma^{(1)}$ and $\sigma^{(2)}$ illustrated in Figure 16.

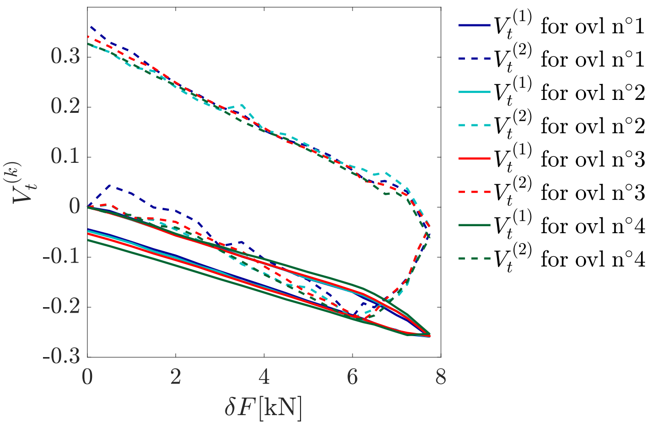

Fig. 19: $V_t^{(k)}$ as a function of δF for all cycles with overload

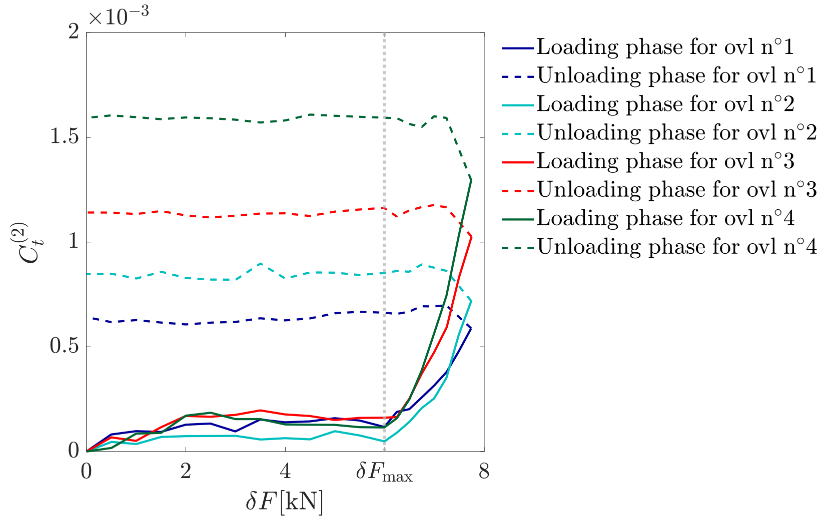

Fig. 20: $C^{(2)}$ as a function δF for all cycles with overload

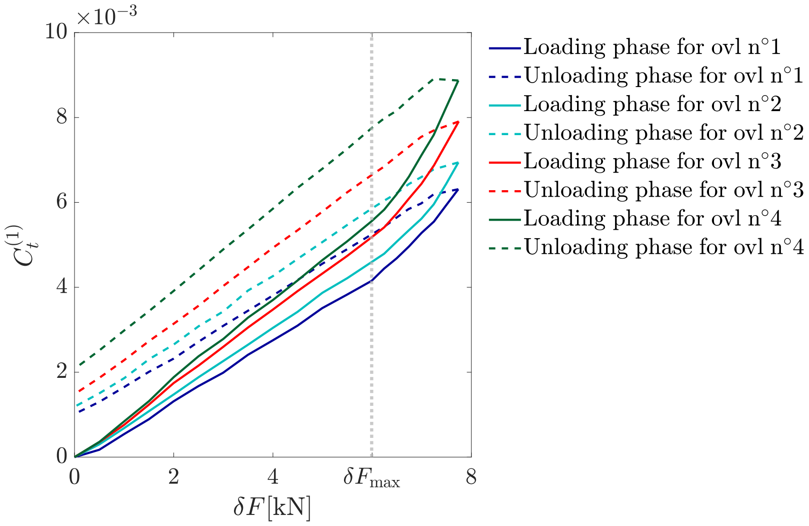

Fig. 21: $C^{(1)}$ as a function δF for all cycles with overload

As a first attempt to improve the level of comprehension, we propose to recombine the two modes $\left(U_f^{(1)}, U_f^{(2)}\right)$ into $\left(\tilde{U}_f^{(1)}, \tilde{U}_f^{(2)}\right)$ so that when $\delta F \leq \delta F_{\max}$ the contribution of $\tilde{U}_f^{(2)}$ remains constant. In other words, the sought recombination of the two modes should allow to align the linear branches of the trajectories in Figure 17 and Figure 18 with the horizontal axis. This recombination simply consists in a rotation of the initial orthogonal basis $\left(U_f^{(1)}, U_f^{(2)}\right)$ within the plane where the data lies on in the crack features space. This rotation is obtained by computing a new SVD on a rectangular matrix containing $\sigma^{(1)}V_t^{(1)}$, $\sigma^{(2)}V_t^{(2)}$ during the unloading phase (the linear branch corresponding to the unloading phase from $\delta F_{\max}$ to 0) as two lines of a rectangular matrix. The two left singular vectors (having two components) are then combined in a 2×2 matrix allowing for rotating from the initial singular vector basis $\left(U_f^{(1)}, U_f^{(2)}\right)$ into a new basis $\left(\tilde{U}_f^{(1)}, \tilde{U}_f^{(2)}\right)$. The evolution of the contribution of these two modified modes is contained into two vectors $C_t^{(1)}, C_t^{(2)}$ resulting from the rotation of $\sigma^{(1)}V_t^{(1)}$, $\sigma^{(2)}V_t^{(2)}$. Figure 20 shows $C_t^{(2)}$ as a function of δF. It is clearly observed that when $\delta F \leq \delta F_{\max}$, $C_t^{(2)}$ remains constant and that a non-linear increases of its amplitude is obtained during the overloading phase of the cycles. This behaviour is as expected and can be interpreted more clearly. This second mode is now only activated in the overloading part of the cycles when $\delta F \geq \delta F_{\max}$. However, Figure 21 shows that the first mode that was expected to depends linearly on δF still evolves non-linearly with respect to δF. Graphically, this can be explained by examining Figure 18. As mentioned earlier, the loading paths in this graph consist in two linear branches for $\delta F \leq \delta F_{\max}$ connected by a curved branch corresponding to the overload phase of the cycle. Roughly speaking, the main orientation of this curved branch is not orthogonal to the two parallel linear branches. However, the decompositions used so far lead orthonormal basis vectors. This means that the projection of the curved branch onto a vector oriented along the linear branches does not vanish. As a consequence the contribution of the first modified mode $\tilde{U}_f^{(1)}$ exhibits the non-linear evolution observed in Figure 21. To further improve the analysis and to try and providing a decomposition of the crack features into two composites features encoding the linear and non-linear evolution of the kinematic field around the crack tip as a function of the applied load, an alternative decomposition is suggested. Following the above described graphical interpretation, the linear / non-linear decomposition should be performed onto a non-orthogonal basis, the first basis vector being aligned with the linear branches and the second one with the main orientation of the curved branch.

For this purpose, the left singular vector U_f^{l} further referred to as *linear* is defined as $\tilde{U}_f^{(1)}$. Then, a linear prediction of $A_{ft'}$ for t' the steps during the unloading phase from $\delta F_{\max}$ to 0 is built. This linear prediction is obtained through an amplitude vector $C_{t'}^{\mathrm{l}} \propto \delta F$ such that at $\delta F = \delta F_{\max}$

$$U_f^{\mathrm{l}} C_{t'}^{\mathrm{l}} \approx A_{ft'}. \tag{13}$$

At this stage, $C_{t'}^{\mathrm{l}}$ is not aimed at reconstructing $A_{ft'}$ accurately but only at giving a linear prediction aligned with U_f^{l}. Then an other SVD is carried out on a residual rectangular matrix A_{ft}^{res} defined as follows:

$$A_{ft}^{\mathrm{res}} = A_{ft} - U_f^{\mathrm{l}} C_t^{\mathrm{l}}. \tag{14}$$

The rank of A_{ft}^{res} can be expected to be the same as that of A_{ft}. However, because of the particular shape of the $\left(V_t^{(1)}, V_t^{(2)}\right)$ trajectories with two parallel linear branches and one curved (but almost linear) branch, and because a linear prediction $U_f^{\mathrm{l}} C_t^{\mathrm{l}}$ along the orientation U_f^{l} of the parallel branches is subtracted from A_{ft}, only one mode is required to accurately reconstruct A_{ft}^{res} as confirmed in Figure 22. The corresponding left singular vector is set as U_f^{nl}. Processing the data as detailed above, one obtains a non-orthogonal basis $\left(U_f^{\mathrm{l}}, U_f^{\mathrm{nl}}\right)$ of the plane previously defined by $\left(U_f^{(1)}, U_f^{(2)}\right)$ or alternatively $\left(\tilde{U}_f^{(1)}, \tilde{U}_f^{(2)}\right)$.

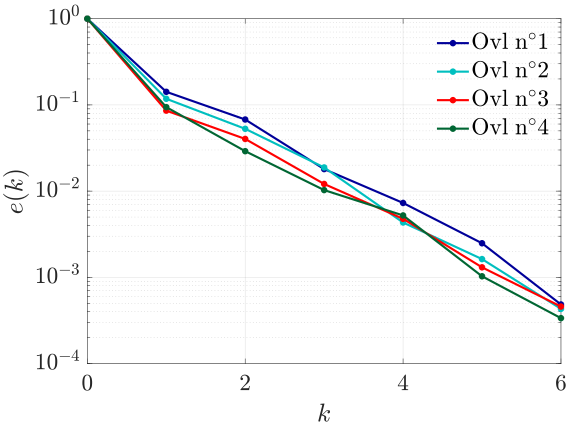

Fig. 22: Relative approximation error for A_{ft}^{res} reconstruction versus the number of terms k

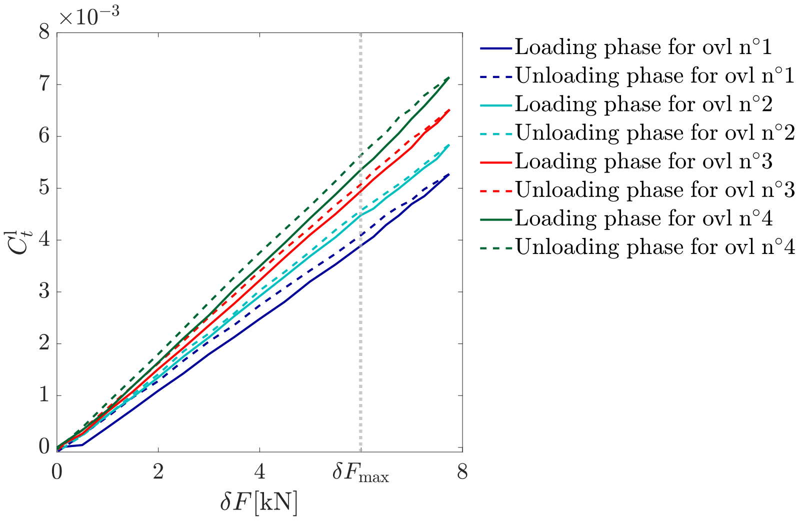

Fig. 23: C_t^{l} as a function of δF for all cycles with overload

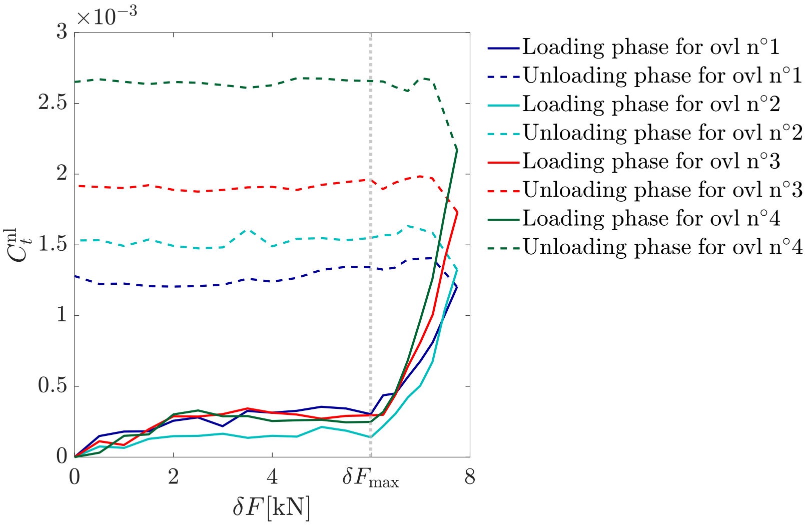

Fig. 24: C_t^{nl} as a function of δF for all cycles with overload

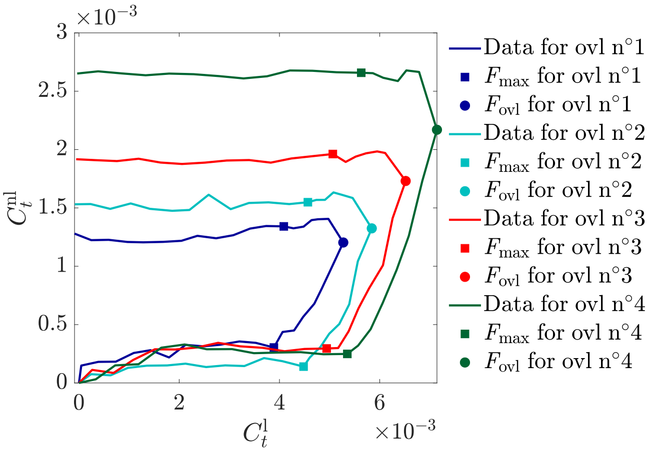

Fig. 25: C_t^{nl} as a function of C_t^{l} for all cycles with overload

Eventually, for any t, A_{ft} is projected onto $(U_f^{\mathrm{l}}, U_f^{\mathrm{nl}})$ leading to the definition of C_t^{l} and C_t^{nl}. Defined as such, $U_f^{\mathrm{l}} C_t^{\mathrm{l}}$, respectively $U_f^{\mathrm{nl}} C_t^{\mathrm{nl}}$, encodes the linear (with respect to δF), respectively non-linear, evolution of A_{ft}. As illustrated in Figure 24, C_t^{nl} exhibits the same behavior as $C_t^{(2)}$ in Figure 20 but as shown in Figure 23, the complementary part encoded in U_f^{l} evolves linearly with respect to δF.

For a deeper understanding, Figure 26 shows the squared coordinates of $\left(U_f^{\mathrm{l}} \text{ and } U_f^{\mathrm{nl}}\right)$ in the normalized crack features basis. Compared to previously obtained basis (see Figure 15), U_f^{l} appears as almost perfectly aligned with the first crack feature ($i.e$ δK_{I}) while for the second vector U_f^{nl} the second and third features contribute significantly. Note the contrary to what was presented in Figure 15, the first feature has the highest amplitude for the second vector. Using these two vectors, Table 4, respectively Table 5, shows the field reconstructed from Williams' basis functions and $U_f^{\mathrm{l}}, U_f^{\mathrm{nl}}$ after rescaling (see Equation 6). As expected from Figure 26, the kinematic fields corresponding to U_f^{l} are similar to that of the Williams' function for $n = 1$. Those of U_f^{nl} behave differently, the main contribution comes from the three crack features represented in the section 3.

Conceptually, U_f^{l} is sough to vary with the crack length and also to depend on the specimen geometry. The amplitude C_t^{l} of its contribution of the kinematic field is linear with respect to δF, this can be interpreted as the effect at the crack tip of remote loading if the material behaves linearly.

Conversely, U_f^{nl} that is activated through C_t^{nl} encompasses the effect of the non-linear constitutive behaviour of the material , activated only during the overload and leading to a residual opening displacement at the end of the cycle. It is expected that the constitutive relation of the material affects not only the evolution of C_t^{nl} with respect to C_t^{l} which can be interpreted as a flow rule (see Figure 25) but also the link between U_f^{nl} and U_f^{l} which one would be more prone to interpret as a yield criterion describing the evolution of the yield surface upon the loading direction (here U_f^{l}). One important remark is also that even if the ratio between F_{ovl} and F_{min} is kept constant all along the experiment, the amplitude of C_t^{nl} is increasing from one overload cycle to the next one, meaning that the main parameter to be considered for characterizing the effect of the overload is rather $\delta_{\mathrm{ovl}} K_I$ or $\delta_{\mathrm{ovl}} K_I - \delta_{\mathrm{max}} K_I$ than $F_{\mathrm{ovl}}/F_{\mathrm{min}}$. Another important remark is that the expected crack closure effect is not observed as such on the kinematic fields. However, the remaining displacement amplitude at the end of the cycle, encoded in the value of C_t^{nl}, is a consequence of the accumulated plastic deformation at the crack tip and that also leads to compressive residual stresses assumed to close the crack. While it is out of the scope of the analysis proposed herein, these residual compressive stresses play a major role in crack retardation during the cycles after the overload. The quantification of the amplitude of non-linear phenomena through the proposed interpretable description can thus be at the basis of a new modeling framework for fatigue overloads and the subsequent retardation effects.

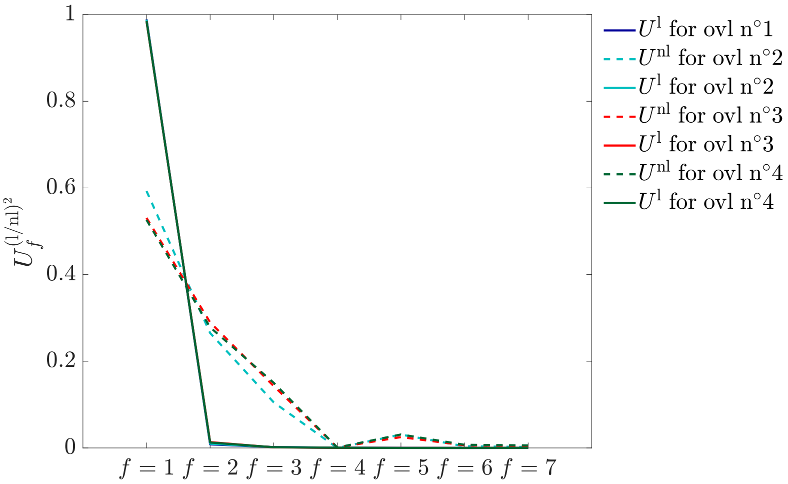

Fig. 26: U_f^{l} and U_f^{nl} for all cycles with overload

Table 4 Displacement field corresponding to the linear $\left(U_f^{\mathrm{l}}\right)$ and the non-linear $\left(U_f^{\mathrm{l}}\right)$ modes of the SVD at δF_{ovl} for the third overload.

	Displacement field reconstruction	
mode	Horizontal component	Vertical component
U_f^{l}	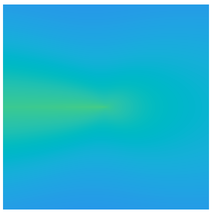	
U_f^{nl}	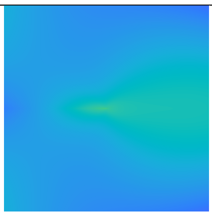	

Table 5 Strain field corresponding to the linear and the non-linear modes of the SVD at δF_{ovl} for the third overload.

	Strain field reconstruction	
mode	ϵ_{xx}	ϵ_{yy}
U_f^{l}	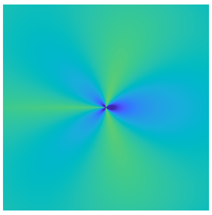	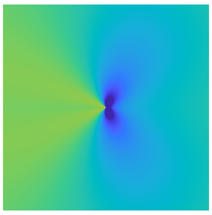
U_f^{nl}	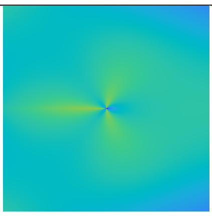	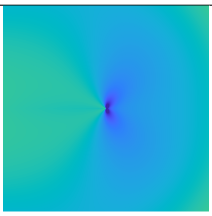

6 Conclusion

In this paper, fatigue tests were conducted on a SENT specimen. Pictures were taken for DIC processing, thus displacement fields were computed. These displacement fields were projected on Williams' series expansion and crack features were extracted. Crack features were analyzed qualitatively in cycle with and without overload, then a quantitative analysis based on SVD analysis provides the most interpretable descriptors for what occurs during overloading. The main observations can be summarized as follows:

- *cycle without overload.* in a case of a cycle without overload all features are proportional thus a single descriptor is required to depict the evolution of the crack tip state. In this case we consider δK_{I}. This observation is consistent with a linear behavior of the specimen.
- *cycle with overload.* In the loading phase (from δF_{min} to δF_{max}) crack features are proportional to the load, then they depict a faster increase than load during the overloading phase (from δF_{max} to δF_{ovl}) making this increase an overload signature. The unloading phase is linear with δF and it maintains almost the same slope as during the loading phase. In the (δK_{I}, δT, δB) space, these crack features are grouped around a plane. We suggested then an SVD analysis to propose an appropriate basis of the crack tip state data structure. The first result of this analysis came with the fact that δK_{I} cannot be considered as the unique descriptor of the kinematic field. We came out with a non-orthogonal basis of composite features $\left(U_f^{\mathrm{l}}, U_f^{\mathrm{nl}}\right)$ that describes the "linear part" through C_t^{l} which vary linearly with respect to δF and the "non-linear" part through C_t^{nl} which is activated only in the overloading phase.

These interpretable composite features can be considered as descriptors of the constitutive behaviour of the crack tip. A clear separation is obtained between the contribution to the kinematic fields around the crack tip having linear elastic response with respect to the applied load and its counterpart with a non-linear and non-elastic behaviour. There is thus all the ingredients to build an effective constitutive model of the crack tip based on the minimum number of interpretable composite features (linear combination of Williams' coefficients).

Acknowledgments

This research was funded, in whole, by the french national research agency (ANR) through grant ANR-20-CE08-0017.

Declarations

Conflict of interest: The authors declare that they have no conflict of interest

Appendix A Crack features from $n = 4$ to $n = 7$

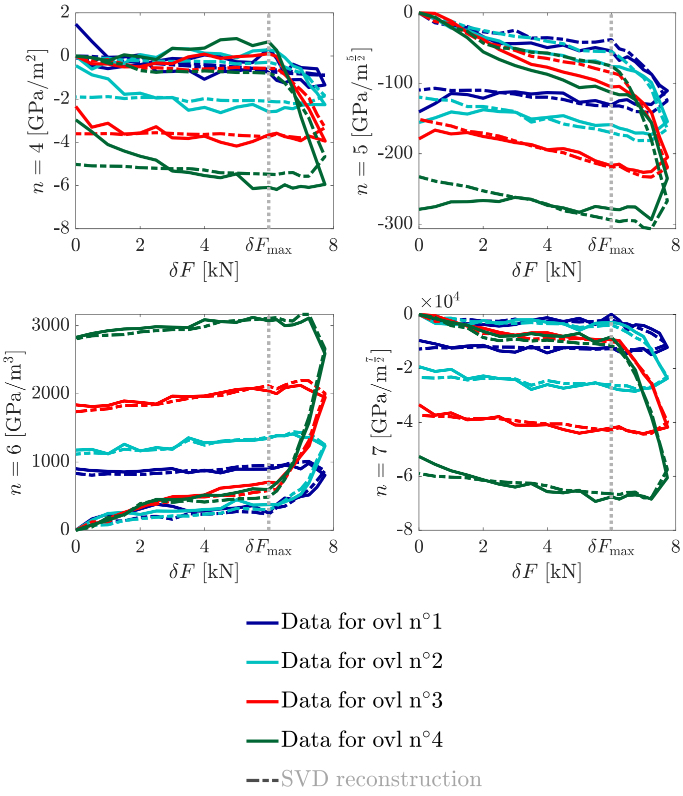

Fig. A1: Crack features from $n = 4$ to $n = 7$ and their SVD reconstruction ($\delta\tilde{K}_{\mathrm{I}}$, $\delta\tilde{T}$ and $\delta\tilde{B}$) as a function of δF for cycles with overload

References

[1] S. Beden, A. Shahrum, and A. K. Ariffin. Review of Fatigue Crack Propagation Models for Metallic Components. *European Journal of Scientific Research*, 2009.

[2] G. Besnard, F. Hild, and S. Roux. "Finite-Element" Displacement Fields Analysis from Digital Images: Application to Portevin–Le Châtelier Bands. *Exp Mech*,

46(6):789–803, December 2006.

[3] R. Hamam, F. Hild, and S. Roux. Stress Intensity Factor Gauging by Digital Image Correlation: Application in Cyclic Fatigue. *Strain*, 43(3):181–192, August 2007.

[4] C. Henninger, S. Roux, and F. Hild. Enriched kinematic fields of cracked structures. *International Journal of Solids and Structures*, 47(24):3305–3316, December 2010.

[5] R.E. Jones. Fatigue crack growth retardation after single-cycle peak overload in Ti-6Al-4V Titanium alloy. *Engineering Fracture Mechanics*, 5:585–604, 1973.

[6] C. Makabe, A. Purnowidodo, and A.J. McEvily. Effects of surface deformation and crack closure on fatigue crack propagation after overloading and underloading. *International Journal of Fatigue*, 2004.

[7] P. Paris and F. Erdogan. A Critical Analysis of Crack Propagation Laws. *Journal of Basic Engineering*, 85(4):528–533, December 1963.

[8] S. Roux and F. Hild. Stress intensity factor measurements from digital image correlation: post-processing and integrated approaches. *Int J Fract*, 140(1-4):141–157, July 2006.

[9] C. Roux-Langlois, A. Gravouil, M.-C. Baietto, J. Réthoré, F. Mathieu, F. Hild, and S. Roux. DIC identification and X-FEM simulation of fatigue crack growth based on the Williams' series. *International Journal of Solids and Structures*, 53:38–47, January 2015.

[10] J. Réthoré. Automatic crack tip detection and stress intensity factors estimation of curved cracks from digital images: Automatic crack tip detection and SIF estimation of curved cracks. *Int. J. Numer. Meth. Engng*, 103(7):516–534, August 2015.

[11] J. Réthoré. UFreckles, October 2018.

[12] A. Saxena, J. D. Landes, J. L. Bassani, and W. Nicoletto. *Fatigue crack-tip mechanics in 7075-T6 aluminium alloy from high-sensitivity displacement field measurements. In: Nonlinear fracture mechanics.*, volume 1. ASTM International, 1988. Google-Books-ID: _X8Epgp8AVsC.

[13] J. Schijve and D. Broek. The Results of a Test Programme Based on a Gust Spectrum with Variable Amplitude Loading. *Aircraft Engng*, 34:314–6, 1962.

[14] D. M. Shuter and W. Geary. Some Aspects of Fatigue Crack Growth Retardation Behaviour Following Tensile Overloads in a Structural Steel. *Fatigue & Fracture of Engineering Materials & Structures*, 19(2-3):185–199, 1996. _eprint:

https://onlinelibrary.wiley.com/doi/pdf/10.1111/j.1460-2695.1996.tb00958.x.

[15] S.S.K. Singh, S. Abdullah, and N. Nikabdullah. The needs of understanding stochastic fatigue failure for the automobile crankshaft: A review. *Engineering Failure Analysis*, 80:464–471, October 2017.

[16] M. Skorupa, A. Skorupa, J. Schijve, T. Machniewicz, and P. Korbut. Effect of specimen thickness and stress ratio on fatigue crack growth after a single overload cycle on structural steel.

[17] C. Sun, Z. Lei, and Y. Hong. Effects of stress ratio on crack growth rate and fatigue strength for high cycle and very-high-cycle fatigue of metallic materials. *Mechanics of Materials*, 69(1):227–236, 2014.

[18] S. Suresh. Micromechanisms of fatigue crack growth retardation following overloads. *Engineering Fracture Mechanics*, 18:577–593, 1983.

[19] C.M. Ward-Close, A.F. Blom, and R.O. Ritchie. Mechanisms associated with transient fatigue crack growth under variable-amplitude loading: An experimental and numerical study. *Engineering Fracture Mechanics*, 32(4):613–638, January 1989.

[20] G. Wild, L. Pollock, A.K. Abdelwahab, and J. Murray. Need for Aerospace Structural Health Monitoring: A review of aircraft fatigue accidents. *International Journal of Prognostics and Health Management*, 12(3), March 2021.

[21] M. L. Williams. On the Stress Distribution at the Base of a Stationary Crack. *Journal of Applied Mechanics*, 24(1):109–114, March 1957.